Tracking the X-ray Polarization of the Black Hole Transient Swift J1727.8–1613 during a State Transition

Adam Ingram,[1] Niek Bollemeijer,[2] Alexandra Veledina,[3,4] Michal Dovčiak,[5] Juri Poutanen,[3] Elise Egron,[6] Thomas D. Russell,[7] Sergei A. Trushkin,[8] Michela Negro,[9] Ajay Ratheesh,[10] Fiamma Capitanio,[10] Riley Connors,[11] Joseph Neilsen,[11] Alexander Kraus,[12] Maria Noemi Iacolina,[13] Alberto Pellizzoni,[6] Maura Pilia,[6] Francesco Carotenuto,[14] Giorgio Matt,[15] Guglielmo Mastroserio,[16] Philip Kaaret,[17] Stefano Bianchi,[15] Javier A. García,[18] Matteo Bachetti,[6] Kinwah Wu,[19] Enrico Costa,[10] Melissa Ewing,[1] Vadim Kravtsov,[3] Henric Krawczynski,[20] Vladislav Loktev,[3] Andrea Marinucci,[21] Lorenzo Marra,[15] Romana Mikušincová,[15] Edward Nathan,[22] Maxime Parra,[23,15] Pierre-Olivier Petrucci,[23] Simona Righini,[24] Paolo Soffitta,[10] James F. Steiner,[25] Jiří Svoboda,[5] Francesco Tombesi,[26,27,28] Stefano Tugliani,[29,30] Francesco Ursini,[15] Yi-Jung Yang,[31,32] Silvia Zane,[19] Wenda Zhang,[33] Iván Agudo,[34] Lucio A. Antonelli,[35,36] Luca Baldini,[37,38] Wayne H. Baumgartner,[17] Ronaldo Bellazzini,[37] Stephen D. Bongiorno,[17] Raffaella Bonino,[29,30] Alessandro Brez,[37] Niccolò Bucciantini,[39,40,41] Simone Castellano,[37] Elisabetta Cavazzuti,[21] Chien-Ting Chen,[42] Stefano Ciprini,[27,36] Alessandra De Rosa,[10] Ettore Del Monte,[10] Laura Di Gesu,[21] Niccolò Di Lalla,[43] Alessandro Di Marco,[10] Immacolata Donnarumma,[21] Victor Doroshenko,[44] Steven R. Ehlert,[17] Teruaki Enoto,[45] Yuri Evangelista,[10] Sergio Fabiani,[10] Riccardo Ferrazzoli,[10] Shuichi Gunji,[46] Kiyoshi Hayashida,[47,*] Jeremy Heyl,[48] Wataru Iwakiri,[49] Svetlana G. Jorstad,[50,51] Vladimir Karas,[5] Fabian Kislat,[52] Takao Kitaguchi,[45] Jeffery J. Kolodziejczak,[17] Fabio La Monaca,[10] Luca Latronico,[29] Ioannis Liodakis,[17] Simone Maldera,[29] Alberto Manfreda,[53] Frédéric Marin,[54] Alan P. Marscher,[50] Herman L. Marshall,[55] Francesco Massaro,[29,30] Ikuyuki Mitsuishi,[56] Tsunefumi Mizuno,[57] Fabio Muleri,[10] Chi-Yung Ng,[31] Stephen L. O'Dell,[17] Nicola Omodei,[43] Chiara Oppedisano,[29] Alessandro Papitto,[35] George G. Pavlov,[58] Abel L. Peirson,[43] Matteo Perri,[36,35] Melissa Pesce-Rollins,[37] Andrea Possenti,[6] Simonetta Puccetti,[36] Brian D. Ramsey,[17] John Rankin,[10] Oliver J. Roberts,[42] Roger W. Romani,[43] Carmelo Sgrò,[37] Patrick Slane,[25] Gloria Spandre,[37] Douglas A. Swartz,[42] Toru Tamagawa,[45] Fabrizio Tavecchio,[59] Roberto Taverna,[60] Yuzuru Tawara,[56] Allyn F. Tennant,[17] Nicholas E. Thomas,[17] Alessio Trois,[6] Sergey S. Tsygankov,[3] Roberto Turolla,[60,19] Jacco Vink,[61] Martin C. Weisskopf[17] And Fei Xie[62,10]

(IXPE Collaboration)

[1] School of Mathematics, Statistics, and Physics, Newcastle University, Newcastle upon Tyne NE1 7RU, UK
[2] Anton Pannekoek Institute for Astronomy, Amsterdam, Science Park 904, NL-1098 NH, The Netherlands
[3] Department of Physics and Astronomy, 20014 University of Turku, Finland
[4] Nordita, KTH Royal Institute of Technology and Stockholm University, Hannes Alfvéns väg 12, SE-10691 Stockholm, Sweden
[5] Astronomical Institute of the Czech Academy of Sciences, Boční II 1401/1, 14100 Praha 4, Czech Republic
[6] INAF Osservatorio Astronomico di Cagliari, Via della Scienza 5, 09047 Selargius (CA), Italy
[7] INAF, Istituto di Astrofisica Spaziale e Fisica Cosmica, Via U. La Malfa 153, I-90146 Palermo, Italy
[8] Special Astrophysical Observatory of the Russian Academy of Sciences, Nizhnij Arkhyz, 369167, Karachayevo-Cherkessia, Russia
[9] Department of Physics and Astronomy, Louisiana State University, Baton Rouge, LA 70803, USA
[10] INAF Istituto di Astrofisica e Planetologia Spaziali, Via del Fosso del Cavaliere 100, 00133 Roma, Italy
[11] Villanova University, Department of Physics, Villanova, PA 19085, USA
[12] Max-Planck-Institut für Radioastronomie, Auf dem Hügel 69, 53121 Bonn, Germany
[13] Agenzia Spaziale Italiana, via della Scienza 5, 09047, Selargius (CA), Italy
[14] Astrophysics, Department of Physics, University of Oxford, Keble Road, Oxford OX1 3RH, UK
[15] Dipartimento di Matematica e Fisica, Università degli Studi Roma Tre, Via della Vasca Navale 84, 00146 Roma, Italy
[16] Dipartimento di Fisica, Università degli Studi di Milano, Via Celoria 16, I-20133 Milano, Italy
[17] NASA Marshall Space Flight Center, Huntsville, AL 35812, USA
[18] X-ray Astrophysics Laboratory, NASA Goddard Space Flight Center, Greenbelt, MD 20771, USA
[19] Mullard Space Science Laboratory, University College London, Holmbury St Mary, Dorking, Surrey RH5 6NT, UK
[20] Physics Department and McDonnell Center for the Space Sciences, Washington University in St. Louis, St. Louis, MO 63130, USA
[21] Agenzia Spaziale Italiana, Via del Politecnico snc, 00133 Roma, Italy
[22] California Institute of Technology, Pasadena, CA 91125, USA
[23] Université Grenoble Alpes, CNRS, IPAG, 38000 Grenoble, France
[24] INAF Institute of Radio Astronomy, Via Gobetti 101, I-40129 Bologna, Italy

[25] Center for Astrophysics, Harvard & Smithsonian, 60 Garden St, Cambridge, MA 02138, USA

[26] Dipartimento di Fisica, Università degli Studi di Roma "Tor Vergata", Via della Ricerca Scientifica 1, 00133 Roma, Italy

[27] Istituto Nazionale di Fisica Nucleare, Sezione di Roma "Tor Vergata", Via della Ricerca Scientifica 1, 00133 Roma, Italy

[28] Department of Astronomy, University of Maryland, College Park, Maryland 20742, USA

[29] Istituto Nazionale di Fisica Nucleare, Sezione di Torino, Via Pietro Giuria 1, 10125 Torino, Italy

[30] Dipartimento di Fisica, Università degli Studi di Torino, Via Pietro Giuria 1, 10125 Torino, Italy

[31] Department of Physics, The University of Hong Kong, Pokfulam Rd, Hong Kong

[32] Laboratory for Space Research, The University of Hong Kong, Cyberport 4, Hong Kong

[33] National Astronomical Observatories, Chinese Academy of Sciences, 20A Datun Road, Beijing 100101, China

[34] Instituto de Astrofísicade Andalucía – CSIC, Glorieta de la Astronomía s/n, 18008 Granada, Spain

[35] INAF Osservatorio Astronomico di Roma, Via Frascati 33, 00040 Monte Porzio Catone (RM), Italy

[36] Space Science Data Center, Agenzia Spaziale Italiana, Via del Politecnico snc, 00133 Roma, Italy

[37] Istituto Nazionale di Fisica Nucleare, Sezione di Pisa, Largo B. Pontecorvo 3, 56127 Pisa, Italy

[38] Dipartimento di Fisica, Università di Pisa, Largo B. Pontecorvo 3, 56127 Pisa, Italy

[39] INAF Osservatorio Astrofisico di Arcetri, Largo Enrico Fermi 5, 50125 Firenze, Italy

[40] Dipartimento di Fisica e Astronomia, Università degli Studi di Firenze, Via Sansone 1, 50019 Sesto Fiorentino (FI), Italy

[41] Istituto Nazionale di Fisica Nucleare, Sezione di Firenze, Via Sansone 1, 50019 Sesto Fiorentino (FI), Italy

[42] Science and Technology Institute, Universities Space Research Association, Huntsville, AL 35805, USA

[43] Department of Physics and Kavli Institute for Particle Astrophysics and Cosmology, Stanford University, Stanford, California 94305, USA

[44] Institut für Astronomie und Astrophysik, Universität Tübingen, Sand 1, 72076 Tübingen, Germany

[45] RIKEN Cluster for Pioneering Research, 2-1 Hirosawa, Wako, Saitama 351-0198, Japan

[46] Yamagata University,1-4-12 Kojirakawa-machi, Yamagata-shi 990-8560, Japan

[47] Osaka University, 1-1 Yamadaoka, Suita, Osaka 565-0871, Japan

[48] University of British Columbia, Vancouver, BC V6T 1Z4, Canada

[49] International Center for Hadron Astrophysics, Chiba University, Chiba 263-8522, Japan

[50] Institute for Astrophysical Research, Boston University, 725 Commonwealth Avenue, Boston, MA 02215, USA

[51] Department of Astrophysics, St. Petersburg State University, Universitetsky pr. 28, Petrodvoretz, 198504 St. Petersburg, Russia

[52] Department of Physics and Astronomy and Space Science Center, University of New Hampshire, Durham, NH 03824, USA

[53] Istituto Nazionale di Fisica Nucleare, Sezione di Napoli, Strada Comunale Cinthia, 80126 Napoli, Italy

[54] Université de Strasbourg, CNRS, Observatoire Astronomique de Strasbourg, UMR 7550, 67000 Strasbourg, France

[55] MIT Kavli Institute for Astrophysics and Space Research, Massachusetts Institute of Technology, 77 Massachusetts Avenue, Cambridge, MA 02139, USA

[56] Graduate School of Science, Division of Particle and Astrophysical Science, Nagoya University, Furo-cho, Chikusa-ku, Nagoya, Aichi 464-8602, Japan

[57] Hiroshima Astrophysical Science Center, Hiroshima University, 1-3-1 Kagamiyama, Higashi-Hiroshima, Hiroshima 739-8526, Japan

[58] Department of Astronomy and Astrophysics, Pennsylvania State University, University Park, PA 16801, USA

[59] INAF Osservatorio Astronomico di Brera, via E. Bianchi 46, 23807 Merate (LC), Italy

[60] Dipartimento di Fisica e Astronomia, Università degli Studi di Padova, Via Marzolo 8, 35131 Padova, Italy

[61] Anton Pannekoek Institute for Astronomy & GRAPPA, University of Amsterdam, Science Park 904, 1098 XH Amsterdam, The Netherlands

[62] Guangxi Key Laboratory for Relativistic Astrophysics, School of Physical Science and Technology, Guangxi University, Nanning 530004, China

ABSTRACT

We report on a campaign on the bright black hole X-ray binary Swift J1727.8–1613 centered around five observations by the Imaging X-ray Polarimetry Explorer (IXPE). This is the first time it has been possible to trace the evolution of the X-ray polarization of a black hole X-ray binary across a hard to soft state transition. The 2–8 keV polarization degree slowly decreased from ∼4% to ∼3% across the five observations, but remained in the North-South direction throughout. Using the Australia Telescope Compact Array (ATCA), we measure the intrinsic 7.25 GHz radio polarization to align in the same direction. Assuming the radio polarization aligns with the jet direction (which can be tested in the future with resolved jet images), this implies that the X-ray corona is extended in the disk plane, rather than along the jet axis, for the entire hard intermediate state. This in turn implies that the long ($\gtrsim$10 ms) soft lags that we measure with the Neutron star Interior Composition ExploreR (NICER) are dominated by processes other than pure light-crossing delays. Moreover, we find that the

evolution of the soft lag amplitude with spectral state differs from the common trend seen for other sources, implying that Swift J1727.8–1613 is a member of a hitherto under-sampled sub-population.

1. INTRODUCTION

Black hole (BH) X-ray binaries display transitions in their X-ray spectrum on timescales of days-months. The *soft state* is dominated by a multi-temperature blackbody component originating from an optically thick, geometrically thin accretion disk (Shakura & Sunyaev 1973; Novikov & Thorne 1973). The *hard state* is instead dominated by a hard power law with high-energy cut off, originating from Compton up-scattering of disk seed photons in a cloud of hot electrons located close to the BH (Thorne & Price 1975; Sunyaev & Truemper 1979), commonly referred to as the *X-ray corona.* The nature of the corona is still an intensely debated topic (Poutanen et al. 2018; Bambi et al. 2021). It has been suggested to be a (patchy) layer located above the disk (the *sandwich model,* Galeev et al. 1979; Haardt & Maraschi 1993; Stern et al. 1995), a large scale height accretion flow inside a truncated disk (the *truncated disk model,* Eardley et al. 1975; Esin et al. 1997; Poutanen et al. 1997) or the (vertically extended or compact) base of the jet (Miyamoto & Kitamoto 1991; Martocchia & Matt 1996; Markoff et al. 2005). Characteristic reflection features including an iron K_α line at $\sim$6.4 keV and a broad Compton hump at $\sim$20–30 keV are also observed (Miller 2007), which result from coronal X-rays irradiating the disk and being reprocessed and re-emitted into the observer's line of sight (Matt et al. 1991; García & Kallman 2010). Although the iron line is narrow in the local restframe, rapid orbital motion and the gravitational pull of the BH distort its shape (Fabian et al. 1989).

Most BH X-ray binaries spend the majority of their time in quiescence and occasionally undergo outbursts of dramatically increased brightness (Done et al. 2007; Tetarenko et al. 2016). The progress of an outburst can be tracked with a hardness intensity diagram (HID), whereby hardness (the ratio of X-ray counts in some harder band to the counts in some softer band) is on the x-axis and X-ray flux is on the y-axis (Homan et al. 2001; Fender et al. 2004). An archetypal outburst traces out a q shape on the HID, moving in an anti-clockwise direction (see Figure 1c for some examples) as it rises

from quiescence, then transitions from hard to soft state via the *intermediate state* and eventually back through the intermediate state to the hard state and finally quiescence (Homan et al. 2005; Belloni 2010).

The X-ray flux displays rapid variability with properties tightly correlated with the spectral changes (van der Klis 2006). In the hard and intermediate states, quasi periodic oscillations (QPOs) are often observed, which appear in the power spectrum as narrow, harmonically related peaks (see Ingram & Motta 2019 for a review). Low frequency QPOs, with frequencies in the range $\sim$0.01–20 Hz, are classified into three categories (Casella et al. 2005). Type-C QPOs are by far the strongest and most commonly observed. They first appear in the hard state superimposed on top of band limited noise that features a roughly constant variability amplitude between low and high frequency breaks. Type-B QPOs are marked by the almost complete disappearance of the band limited noise. The presence of either Type-C or Type-B QPOs is used to sub-classify the intermediate state into respectively the hard intermediate state (HIMS) and soft intermediate state (SIMS). The soft state features a very low level of variability, except for occasional QPOs including Type-A QPOs, which are fairly broad and weak. Whereas the spectral evolution tracked by the HID can vary from source to source, or even from outburst to outburst of a given source (e.g. Dunn et al. 2010), the evolution of the band limited noise appears to be universal and can be tracked with just one parameter – the power spectral hue (Heil et al. 2015a). This describes the relative amplitude of the power spectrum in four broad 'power-color' frequency bands (see Section 4.2 for a detailed explanation).

Time lags between variations of the flux in different energy bands can be measured using the cross spectrum (van der Klis et al. 1987). The time lags measured from the cross-spectrum are a function of Fourier frequency, enabling lags between variations on different characteristic variability timescales to be separated out. At low Fourier frequencies (long variability timescales), variations in hard X-rays are observed to lag those in soft X-rays (so called hard lags; Miyamoto et al. 1988; Nowak et al. 1999). This is commonly attributed to inward propagation of accretion rate fluctuations (Lyubarskii
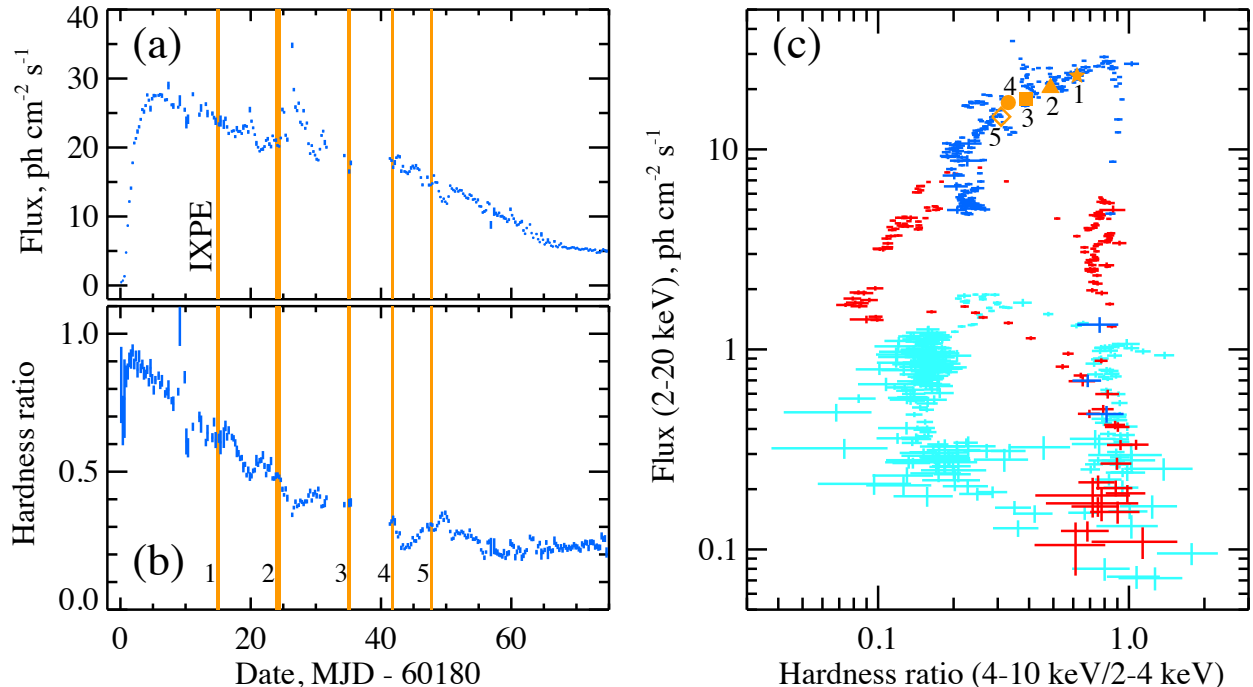
Figure 1. Evolution of X-ray properties of Swift J1727.8–1613 during the outburst, determined with MAXI (Matsuoka et al. 2009). Vertical orange strips show the times of IXPE observations. (a) MAXI light curve in the 2–20 keV range. (b) Hardness ratio of the photon flux in the 4–10 keV band to that in the 2–4 keV band. (c) Hardness-intensity diagram. Blue crosses show the evolution of Swift J1727.8–1613 during the current outburst. The positions of the source on the diagram during five IXPE observations are numbered and marked with orange symbols. For comparison, we also plot the time evolution of MAXI J1820+070 during its 2018 outburst with red crosses and GX 339−4 during its 2010 outburst with the cyan crosses. This plot is designed as an update of Figure 1 in Veledina et al. (2023).

1997; Kotov et al. 2001; Arévalo & Uttley 2006; Ingram & van der Klis 2013), but has been alternatively interpreted as light crossing lags between successive Compton scattering orders in a highly extended corona (e.g. Kazanas et al. 1997; Reig & Kylafis 2015) or as spectral evolution during X-ray flares (Poutanen & Fabian 1999; Körding & Falcke 2004). At high Fourier frequencies ($\nu \gtrsim 1 - 10$ Hz, short variability timescales), soft lags are instead observed (Uttley et al. 2011; De Marco et al. 2015, 2017). The soft lags are typically attributed to *reverberation* (Reynolds et al. 1999; Poutanen 2002; Uttley et al. 2014), in that reflected photons take a longer path to the observer than directly observed photons, and the reflection spectrum includes a soft excess. The soft lags follow a common evolution with power spectral hue across the population of BH X-ray binaries that sees them sharply increase during the HIMS from as low as ~ 0.5 ms to as high as 100 ms (Wang et al. 2022). Under the reverberation interpretation, this would require the vertical extent of the corona to dramatically increase during the HIMS (De Marco et al. 2021), which Wang et al. (2021) suggested may be causally connected to the discrete jet ejections observed at radio wavelengths days later. However, other processes may contribute to,

and may even dominate, the soft lag signal, including a complex interplay of broadband spectral components (Veledina 2018; Kawamura et al. 2023). Further information is therefore required to determine the relative importance of light-crossing delays and other processes.

The Imaging X-ray Polarimetry Explorer (IXPE; Weisskopf et al. 2022) now enables sensitive X-ray polarimetry, providing a novel diagnostic of the coronal geometry and its evolution with spectral state. In energy bands in which we see photons after multiple Compton up-scatterings, the net polarization of the optically-thin corona aligns with its minor axis, such that, for example, a horizontally extended corona will be vertically polarized (Poutanen & Svensson 1996; Ursini et al. 2022). This is because photons propagating horizontally have a higher chance being scattered and polarization is dominated by those scattered 'sideways' at about 90° having the electric vector perpendicular to the scattering plane, i.e. in the vertical direction. The first BH X-ray binary to be observed in the hard state was Cyg X-1 (Krawczynski et al. 2022). The 2–8 keV polarization was found to align with the radio jet (Miller-Jones et al. 2021), indicating that the corona is extended radially in the disk plane during the hard state. Thus, if the

sharp increase in soft lag magnitude during the HIMS is caused by the corona switching from radially extended in the disk plane (scale height $H/R < 1$) to highly vertically extended along the jet axis ($H/R \gg 1$), then we would expect the polarization angle (PA) to flip during the HIMS. However, no such flip was observed when Cyg X-1 was later observed in the soft state (Dovciak et al. 2023, Steiner et al., in prep.). The coronal emission, which was still strong in the IXPE band, remained aligned with the radio jet. However, the source was not observed in the HIMS during a transition, it was only observed first in the hard state then later in the soft state. Moreover, Cyg X-1 is a persistent source that does not exhibit the usual outburst behaviors such as a q-shaped HID and prominent QPOs. 4U 1630-47 has also been observed in two states, but these were the soft state (Ratheesh et al. 2023) and the 'steep power law' or 'very high' state (Rodriguez Cavero et al. 2023), which is observed reasonably rarely (Remillard & McClintock 2006). The first source that has enabled IXPE to track the X-ray polarization across a state transition is Swift J1727.8–1613.

Swift J1727.8–1613 was discovered on 2023 Aug 24 (Kennea & Swift Team 2023; Negoro et al. 2023) when it entered a very bright outburst initially reaching ∼7 Crab in the 2–20 keV band. All of the source properties strongly point to its identification as a BH X-ray binary, including its X-ray spectrum (Liu et al. 2023b; Sunyaev et al. 2023), the detection of Type-C QPOs (Palmer & Parsotan 2023; Draghis et al. 2023; Bollemeijer et al. 2023; Mereminskiy et al. 2023), and of flat spectrum radio emission indicative of a compact jet (Miller-Jones et al. 2023b; Bright et al. 2023). IXPE first observed Swift J1727.8–1613 on 2023 Sept 7 and measured a polarization degree (PD) of $4.1\% \pm 0.2\%$ and a PA of $2^\circ.2 \pm 1^\circ.3$ (Veledina et al. 2023), which is roughly in the North-South direction. This aligns with the sub-mm polarization (PA$=-4^\circ.1 \pm 3^\circ.5$, Vrtilek et al. 2023), and the optical polarization (Kravtsov et al. 2023). Resolved jet images are not yet available, but using the sub-mm polarization as a proxy suggests that the 2–8 keV polarization again aligns with the jet.

In this paper, we present four further IXPE observations of Swift J1727.8–1613 during a hard to soft state transition and place them in the context of complimentary monitoring by the Neutron star Interior Composition ExploreR (NICER; Gendreau et al. 2016) and several radio facilities. We detail our observations and data reduction procedures in Section 2, present X-ray polarization results in Section 3, and compare with X-ray timing and radio properties in Section 4. We then dis-

Table 1. IXPE observation log.

Obs	OBSID	Start UTC	End UTC	Live time ks
1	02250901	Sept 07 19:35	Sept 08 06:36	19.0
2	02251001	Sept 16 17:15	Sept 17 13:29	37.0
3	02251101	Sept 27 22:15	Sept 28 09:51	21.0
4	02251201	Oct 04 12:57	Oct 04 23:58	17.5
5	02251301	Oct 10 11:30	Oct 10 22:39	17.8

cuss our results and conclude in Sections 5 and 6, respectively.

2. OBSERVATIONS AND DATA REDUCTION

We consider five observations of Swift J1727.8–1613 between 2023 September 7 and 2023 October 10 (Table 1) in the context of coverage by NICER and several radio facilities. Figures 1a,b show the timing of the IXPE observations with respect to the source flux variations and the hardness ratio as measured by MAXI (Matsuoka et al. 2009).[1] Figure 1c places the observations on an HID, indicating that they cover the hard to soft state transition.

2.1. IXPE Data Reduction

IXPE is the first satellite mission dedicated to X-ray polarimetry in the 2–8 keV band (Weisskopf et al. 2022). It carries three X-ray telescopes, each made of a Mirror Module Assembly (Ramsey et al. 2022) and a polarization-sensitive gas-pixel detector unit (Soffitta et al. 2021; Baldini et al. 2021), that enable imaging X-ray polarimetry of extended sources and a huge increase of sensitivity for point-like sources. IXPE has an angular resolution of $\lesssim 30''$ (half-power diameter, averaged over the three detector units). The overlap of the fields of view of the three detector units is circular with a diameter of $9'$; spectral resolution is better than 20% at 6 keV.

We downloaded level 2 data from the IXPE archive at the HEASARC[2] and analyzed it with IXPEOBSSIM version 30.6.2 (Baldini et al. 2022) and HEASOFT/XSPEC version 12.13.1d (Arnaud 1996). All IXPE observations were carried out with the 'gray' filter in front of the detector units (DUs) (Ferrazzoli et al. 2020; Soffitta et al. 2021). This reduces the incident count rate by a factor of ~ 10 to reduce the effects of dead-time (which is

[1] http://maxi.riken.jp/

[2] https://heasarc.gsfc.nasa.gov/docs/ixpe/archive/

~ 1.2 ms) and to enable all of the data to be transmitted within the allocated telemetry. Despite its name, the filter is dependent on photon energy, with transmission dropping sharply at low energies. Specific response matrices therefore must be used for observations utilizing the gray filter, which are available both in the IXPEOBSSIM package and in the HEASARC CALDB.

Following Veledina et al. (2023), we measure polarization only by fitting weighted I, Q, and U spectra (created using the `pha` algorithm of IXPEOBSSIM) with simple phenomenological models in XSPEC, and not using the `pcube` algorithm of IXPEOBSSIM. This method properly takes into account the energy response of the instrument, which is important due to the steep drop in filter transmission at low energies. We fit spectropolarimetric models separately to the three DUs, and combine them for plotting purposes only.

For polarimetry, we extract events from a circular region with $80''$ radius centered on the source. No background subtraction is necessary for sources as bright as Swift J1727.8–1613, since in this case the IXPE background is dominated by scattered source emission, even at large offset (hence, the instrumental background itself is negligible and can be ignored, Di Marco et al. 2023). For timing analysis, we instead use a $180''$ radius to maximize counts without including events from the detector edges.

2.2. NICER data reduction

We analyze four sets of NICER observations of Swift J1727.8–1613 that were performed before and on the same days as IXPE observations 1, 2, and 4 (Swift J1727.8–1613 was not visible to NICER during IXPE observations 3 and 5). NICER is an X-ray telescope with excellent timing capabilities located on the International Space Station (ISS), and it is sensitive to X-rays in the 0.2–12 keV range. The ObsIDs of the data used are 620980104 on August 28, 6750010501 and 6750010502 on September 7 and 8, 6557020201 and 6557020202 on September 16 and 17, and 6557020401 on October 4. We downloaded these data from the NICER archive on the HEASARC website.[3] NICER detects X-rays with individual detectors and consists of 7 Modular Power Units (MPUs), each consisting of 8 Focal Plane Modules (FPMs), for a total of 56 detectors, of which 52 have been functional after its launch. The very high source count rates from Swift J1727.8–1613 can cause internal telemetry saturation when all FPMs are turned on, resulting in many very short 'shredded' Good Time

Intervals (GTIs) and preventing reliable timing analysis.[4] To mitigate this effect, a reduced number of 17 FPMs were active on August 28 and October 4, 12 FPMs on September 7 and 8, and 10 FPMs on September 16 and 17, which resulted in several hundred seconds of usable data for each ISS orbit. In some orbits, the number of FPMs was reduced even further. We excluded those orbits from our analysis.

NICER has suffered from a light leak problem since 2023 May 22, which increases background noise for observations taken during orbit day, when solar light reaches the X-ray detectors. Detector resets known as undershoots, which are a regular feature of a functioning FPM, happen much more often due to the solar light and can then cause degraded spectral resolution and increased noise levels at low energies.[5] The data were reprocessed with the `nicerl2` pipeline from NASA's HEASoft (v6.32.1) (HEASARC 2014), released on 2023 August 23, with the recommended and most up-to-date filter columns settings. We used the default undershoot rate criterion of 500 cnt s^{-1} for all ObsIDs except 6557020201 and 6557020202, for which we manually set that threshold to 800 cnt s^{-1}. We do note that doing so increases the systematic errors on any spectral or timing results from these data, and take extra care in interpreting our results. Otherwise, we followed the recommendations on the HEASARC website. For parts of the NICER timing analysis, we make use of the STINGRAY libraries (Huppenkothen et al. 2019a,b; Bachetti et al. 2023).

2.3. Radio Data Reduction

The RATAN-600 radio telescope observed daily at 4.7, 8.2 and 11.2 GHz. Observations were performed using the 'Southern sector and Flat mirror' antenna from 2023 September 14 up to September 30, then with the 'Northern sector' (which has a higher sensitivity) from October 1 until October 20. Additional observations at 22.3 GHz were carried out during radio flares. The data were calibrated with the quasar 3C 161 (J0627−05), included in the radio flux scale by Ott et al. (1994).

The Medicina 32-m radio telescope performed observations (quasi-)simultaneously with the IXPE sessions on 2023 September 15, 28, and October 3 at 8.4 and 24.2 GHz, depending on the weather and radio interference conditions. We also carried out additional sessions in order to better follow the evolution of the radio flux

---

[3] https://heasarc.gsfc.nasa.gov/docs/nicer/archive/

[4] https://heasarc.gsfc.nasa.gov/docs/nicer/analysis_threads/heasoft632/

[5] https://heasarc.gsfc.nasa.gov/docs/nicer/analysis_threads/undershoot-intro/
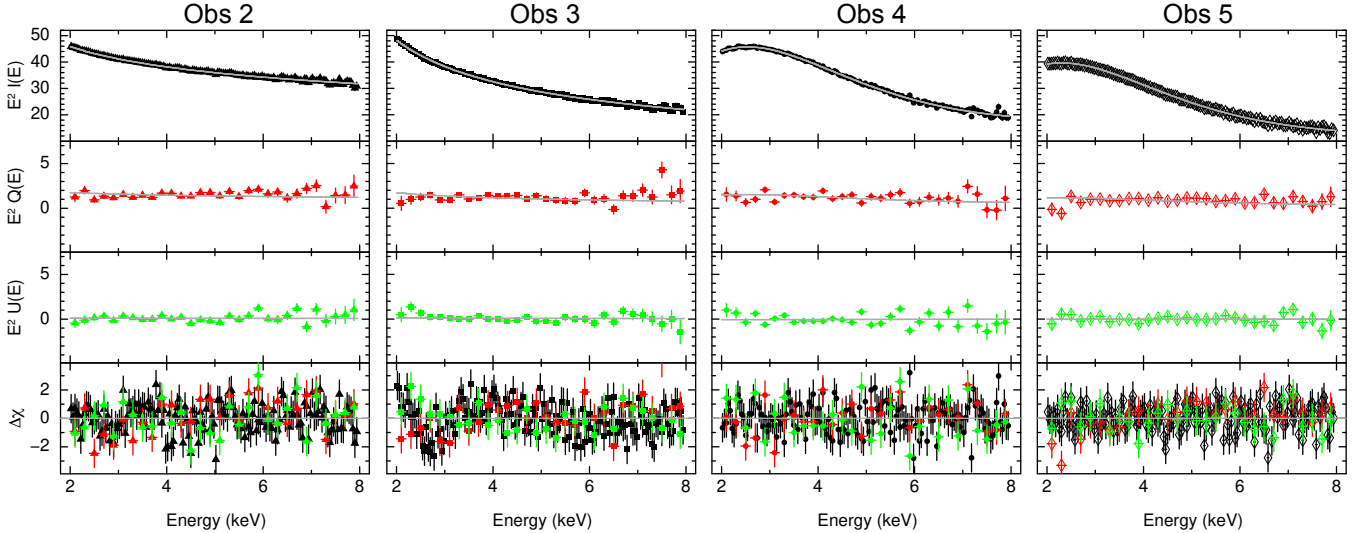
Figure 2. Spectro-polarimetric fits for IXPE observations 2–5 (a similar plot for observation 1 can be found in Figure 2 of Veledina et al. 2023). The top three panels show unfolded IXPE Stokes I (black), Q (red), and U (green) spectra (as labeled), in units of keV cm^{-2} s^{-1}, along with the best-fit `polconst` model in gray (`polconst*powerlaw` for observations 1–3 and `polconst*[diskbb+powerlaw]` for observations 4–5). The bottom panel shows the residuals in terms of contributions to the fit statistic χ. The three IXPE DUs are grouped together for plotting purposes, but are treated separately in the fit. Data are also re-binned in energy for plotting purposes only (XSPEC command `setplot rebin 10.0 5`).

density. We applied gain curve and pointing offset corrections to the measurements. The data were calibrated by performing cross-scans on NGC 7027 and 3C 48. The data analysis was performed with the SINGLE-DISH-IMAGER (SDI; Egron et al. 2017), a software designed to perform automated baseline subtraction, radio interference rejection and calibration.

The Australia Telescope Compact Array (ATCA) observed at 5.5 and 9 GHz on 2023 September 28, coinciding with a portion of IXPE observation 3. These observations were taken under project code C2601 as part of a large radio monitoring campaign of Swift J1727.8–1613. ATCA was in a compact H168 configuration,[6] consisting of 5 antennas in a compact core, and a single, isolated antenna 6 km away. We used PKS B1934−638 and PKS B1730−130 for primary and secondary calibration, respectively. The data were analyzed and imaged using standard procedures within the Common Astronomy Software Applications for Radio Astronomy (CASA, version 5.1.3; CASA Team et al. 2022). The full radio campaign will be presented in a future paper.

The 100-m telescope at Effelsberg observed on 2023 September 28, October 10, and October 15 at 5.5 and 14.4 GHz. The values were corrected for atmospheric attenuation and the gain-elevation effect. The final cali-

bration in Jy was done with the flux density calibrators 3C 286 and NGC 7027. Details of the analysis procedure are described e.g. in Kraus et al. (2003)

3. X-RAY POLARIZATION RESULTS

We measure the PD and PA by fitting phenomenological models in XSPEC to the Stokes I, Q, and U spectra of all four observations. We first use the multiplicative `polconst` model to impart a constant PD and PA to the entire Stokes I spectral model. In line with what found for observation 1 (Veledina et al. 2023), we find that we cannot constrain line of sight absorption models for any of the observations, with the best-fit hydrogen column density always tending to zero. Also in agreement with Veledina et al. (2023), we find that the `gain fit` functionality of XSPEC is required to circumvent calibration issues. The full model we fit to all of the observations is

$$\texttt{polconst*constant*(diskbb+powerlaw)}. \quad (1)$$

Here, the constant accounts for the different absolute flux calibration of the different DUs. We freeze it to unity for DU1 and leave it as a free parameter for DU2 and DU3. `diskbb` is a multi-temperature disk blackbody with peak temperature kT_{in} and normalization norm$_d$, and `powerlaw` models the specific photon flux as norm$_{po} \times E^{-\Gamma}$ photons cm^{-2} s^{-1} keV^{-1}. For each observation, we test whether both components are needed with an F-test.

---

[6] https://www.narrabri.atnf.csiro.au/operations/array_configurations/configurations.html

Table 2. Results of polarimetric and timing analyses of the five IXPE observations.

Parameter	Units	Obs 1	Obs 2	Obs 3	Obs 4	Obs 5
			polconst * (diskbb+powerlaw)			
PD	%	4.1 ± 0.2	3.9 ± 0.1	3.6 ± 0.2	3.3 ± 0.2	2.9 ± 0.2
PA	deg	2.2 ± 1.3	1.8 ± 1.1	2.1 ± 1.6	-1.1 ± 1.8	-0.5 ± 2.3
$\chi^2/$dof		1282/1329	1340/1329	1306/1329	1327/1327	1267/1327
			pollin * (diskbb+powerlaw)			
PD_5	%	4.3 ± 0.2	4.3 ± 0.2	4.1 ± 0.3	3.8 ± 0.3	3.8 ± 0.3
PD_{slope}	%	0.3 ± 0.2	0.5 ± 0.1	0.6 ± 0.2	0.5 ± 0.2	0.9 ± 0.2
PA	deg	2.0 ± 1.3	1.9 ± 1.1	1.6 ± 1.6	-1.4 ± 1.8	-0.6 ± 2.2
$\chi^2/$dof		1277/1328	1321/1328	1297/1328	1321/1326	1252/1326
F-test	σ	2.2	4.4	3.1	2.5	4.0
			Timing			
ν_{qpo}	Hz	1.349 ± 0.003	2.788 ± 0.008	4.16 ± 0.04	$6.7^{+0.1}_{-0.2}$	8.0 ± 0.3
$HWHM_{qpo}$	Hz	0.126 ± 0.004	0.28 ± 0.01	0.52 ± 0.06	0.38 ± 0.37	$0.43^{+0.35}_{-0.38}$
ν_{2qpo}	Hz	2.66 ± 0.026	5.55 ± 0.07	$\equiv 2\nu_{qpo}$	$\equiv 2\nu_{qpo}$	$\cdots$
$HWHM_{2qpo}$	Hz	0.37 ± 0.09	$\equiv 2HWHM_{qpo}$	$\equiv 2HWHM_{qpo}$	$\equiv 2HWHM_{qpo}$	$\cdots$
$\chi^2/$dof		101/84	127/88	112/91	38/50	41/49
$hue_{(2-8keV)}$	deg	137.6 ± 1.7	179.8 ± 2.1	185.7 ± 3.3	201.5 ± 7.6	209 ± 11
$hue_{(5-8keV)}$	deg	147.6 ± 6.9	180.8 ± 9.3	185.6 ± 15	$\cdots$	$\cdots$

NOTE—Spectral and calibration parameters used for the spectro-polarimetric fits are presented in Appendix A. We quote the reduced χ^2 of the two spectro-polarimetric models, and the results of an F-test comparison between the two. For the timing analysis, we quote the centroid and width of the QPO fundamental and second harmonic, the reduced χ^2 values of the multi-Lorentzian fits used to determine them, and the power spectral hue measured in two energy bands (2–8 keV and 5–8 keV). For observations 4 and 5, the power spectral hue is unconstrained in the 5–8 keV band.

We find that only a power law is required for observations 1–3, whereas both disk and power law contributions are required for observations 4–5. We note that this is an oversimplified model, with the true source spectrum very likely also containing reflection features, but we are often unable to detect these with IXPE given its limited band pass. We also note that the simplicity of the model does not affect the polarization measurement, which is of primary interest here. Since we are only trying to measure the PD and PA of the combined model, and are not attempting to separate into components each with its own polarization, all that matters is the goodness of fit. We will leave a joint spectral fit considering multiple observatories to a later paper.

We find good fits for all five observations. Figure 2 shows the I, Q, and U spectra alongside the best-fit model. The bottom panel demonstrates that there are no structured residuals. The spectral parameters of the phenomenological model used, plus the calibration parameters used, are quoted in Appendix A. Table 2 lists the best-fit PD and PA alongside the corresponding re-
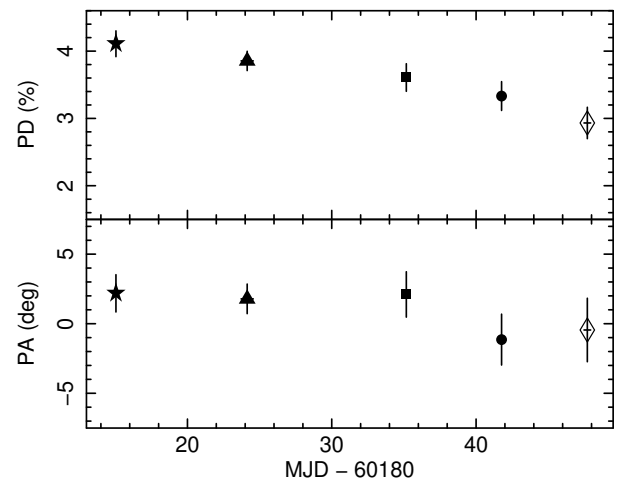

Figure 3. Variation of the PD (top) and PA (bottom) in the 2–8 keV range for the five IXPE observations.

duced χ^2 values. The 2–8 keV polarization is detected with high significance for all observations. As can be seen most clearly in Figure 3, the PA is consistent with
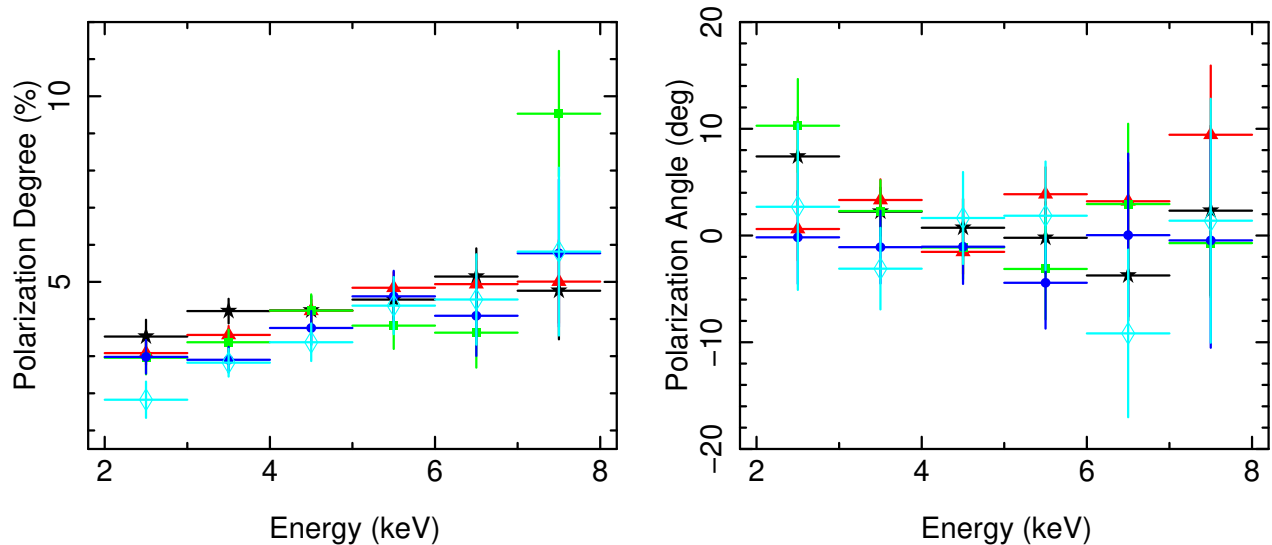
Figure 4. PD (left) and PA (right) as a function of energy for observations 1 (black stars), 2 (red triangles), 3 (green squares), 4 (blue circles) and 5 (cyan diamonds). Error bars are 68% confidence.

remaining unchanged across all observations but the PD appears to systematically decrease with time.

We test if the PD is statistically required to change with time by comparing the sum of the best-fit `polconst` models presented in Table 2 ($\chi^2/\text{dof} = 6523/6641$) to alternatives with PD and/or PA tied to be the same across all five observations. We find that holding PA constant in time but allowing PD to vary yields a better fit ($\chi^2/\text{dof} = 6526/6645$, thus a slightly higher null-hypothesis probability). Allowing the PA to change between observations 3 and 4 but stay otherwise constant (motivated by the final two PA values in Figure 3 appearing to be $\sim 2°$ smaller than the first three) yields no significant improvement to the fit ($\chi^2/\text{dof}=6523/6644$). We therefore conclude that PA is indeed consistent with being constant in time. Holding both PD and PA constant in time gives $\chi^2/\text{dof} = 6546/6649$. Using an F-test, we find that the model with varying PD and constant PA is preferred to the model with constant PD and PA with 3.5 σ confidence.

To investigate the energy dependence of the polarization, we first freeze all parameters except for PD and PA, and conduct a series of fits that each only consider one of six 1-keV wide energy ranges; i.e. we first fit only in the 2–3 keV range, then only in the 3–4 keV range, and so on. The resulting energy dependent PD and PA values are plotted in Figure 4. The PD appears to increase with energy, with the PA consistent with being independent of energy. To test this statistically, we instead fit the model

$$\texttt{pollin*constant*(diskbb+powerlaw)}, \qquad (2)$$

in the 2–8 keV band. The `pollin` model sets $\text{PD}(E) = \text{PD}_1 + \text{PD}_{\text{slope}}(E - 1\,\text{keV})$ and $\text{PA}(E) = \text{PA}_1 + \text{PA}_{\text{slope}}(E - 1\,\text{keV})$. We find that allowing PA_{slope} to be a free parameter yields no significant improvement in χ^2 over freezing it to zero, thus we fix $\text{PA}(E) = \text{PA}_1 = \text{PA}$ hereafter. We replace the constant PD_1, which is the PD at 1 keV, with another parameter PD_5, which is the PD at 5 keV. This is so that the constant we fit for corresponds to the PD at an energy within the IXPE bandpass.[7] The two are simply related by $\text{PD}_1 = \text{PD}_5 - 4\,\text{PD}_{\text{slope}}$. The best-fit parameters and goodness of fit of the `pollin` model are also quoted in Table 2. The spectral parameters of the two models are identical within our chosen rounding convention. We see that the `pollin` model is preferred with $> 3\sigma$ significance for observations 2, 3, and 5, meaning we can conclude with high statistical confidence that PD increases with energy in these three observations.

We finally test if the slope of PD with energy changes over the five observations. The `pollin` model with PD_5, PD_{slope} and PA free to vary between observations (as in Table 2) has $\chi^2/\text{dof} = 6469/6636$. We find that an alternative model with PD_5 and PA tied across observations gives a statistically more favorable fit with $\chi^2/\text{dof} = 6476/6644$. An F-test comparison between this best-fit model and an alternative with all three parameters constant in time ($\chi^2/\text{dof} = 6489/6648$) indicates that the varying slope model is preferred with 2.6σ

---

[7] To do this, we define a dummy parameter in XSPEC that takes the value of PD_5.
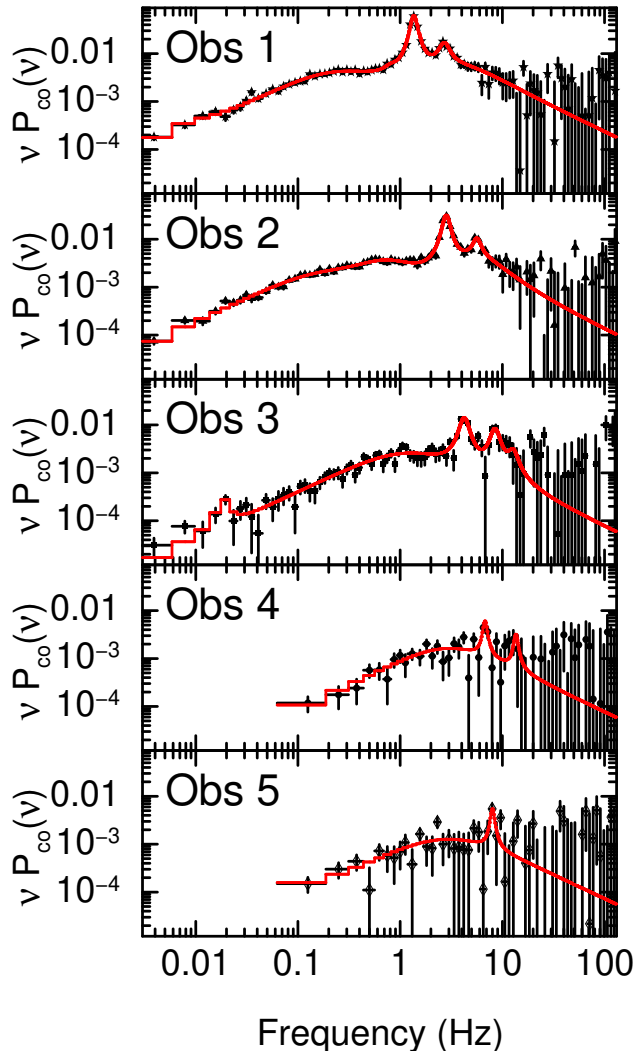
Figure 5. Power spectrum of the five IXPE observations, estimated from the co-spectrum of the DU1+DU2 light curve crossed with the DU3 light curve. The best-fit multi-Lorentzian model is shown in red. The 2–8 keV energy band is used for observations 1–3, and the 2–5 keV band for observation 4–5.

confidence. The variation in slope with time is therefore only marginally significant.

4. TIMING ANALYSIS

4.1. *IXPE Power Spectrum*

Figure 5 shows a 2–8 keV power spectrum for each of the five IXPE observations. They were calculated by taking the co-spectrum between independent detectors, following Bachetti et al. (2015) and Ewing et al (in prep). This method enables us to estimate the power spectrum with no contribution from Poisson noise, thus circumventing the need to model the dead-time-affected Poisson noise contribution. Dead-time is the time after

each photon is detected during which another photon cannot be detected. For IXPE this time is ~ 1.2 ms, which is relatively large. We first extract two statistically independent light curves with time bins of duration $dt = 1/256$ s: one by summing photons from DU1 and DU2, and the other only using DU3 photons. We then calculate the cross-spectrum between the two light curves. To ensure Gaussian distributed uncertainties (see van der Klis 1989; Barret & Vaughan 2012), we ensemble average over segments of length $T_{\rm seg}$ and employ geometric frequency re-binning with re-binning constant $c = 1.08$ (Ingram 2012). The co-spectrum is the real part of this cross-spectrum.

For observations 1–3, we ensemble average using $T_{\rm seg} = 256$ s. Strong, harmonically related peaks can clearly be seen in the resulting co-spectra. These are Type-C QPOs, with centroid frequency increasing during the hard to soft transition in line with known phenomenology (Wijnands et al. 1999; Belloni 2010; Ingram & Motta 2019). For observations 4–5, we instead use $T_{\rm seg} = 8$ s to achieve adequate signal to noise. Using shorter segments leads to less data being discarded due to full segments not fitting into short good time intervals, and the trade-off is losing access to Fourier frequencies below $1/T_{\rm seg}$. The total number of segments averaged over for Obs 1–5 is respectively 67, 117, 70, 2329 and 2297, with the much larger values for the final two observations being due to the much shorter segment length employed (there are 58 and 50 segments of length 256 s in observations 4 and 5 respectively). We still see QPO features consistent with a Type-C classification in these final two observations, but they are only marginally significant ($2.8\,\sigma$ in both cases) due to far lower signal to noise. Nonetheless, the QPO in observation 4 is confirmed by inspection of the power spectra of the simultaneous NICER observations, in which the QPO features are still very clear. There is no NICER coverage of observation 5 due to Sun constraints.

We model each co-spectrum with a multi-Lorentzian model (e.g. Psaltis et al. 1999; van Straaten et al. 2002). We use six Lorentzian functions for observation 1, five for observations 2–3, and three for observations 4–5. We decide on the number of Lorentzians using F-tests, with each component being required to improve the fit with $> 2\sigma$ significance. The red lines in Figure 5 represent the best-fit models. The measured QPO frequencies, their half width at half maximum (HWHM) values, and the reduced χ^2 of the fit are listed in Table 2. Subscripts 'qpo' and '2qpo' correspond respectively to the first (fundamental) and second harmonic. For observation 1, the signal to noise is high enough for us to leave the centroid and width of both QPO components free,

with the second harmonic consistent with being double that of the first. For other observations, we require the width and/or centroid of the second harmonic to be double that of the fundamental, again using an F-test to decide. A third harmonic can be seen in observation 3. We find that the statistically preferred fit is achieved by tying the centroid and FWHM of this component to be triple that of the fundamental. No second harmonic is detected in observation 5.

Our model for observation 3 includes another QPO feature at 18.4 ± 1.2 mHz. This feature is marginally significant (1% null hypothesis probability according to an F-test), but could be instrumental since IXPE undergoes dithering on three periods: 107, 127, and 900 s (Ewing et al., in prep.). The ~ 18 mHz feature could therefore be the second harmonic of the 107 s dithering period. This hypothesis is difficult to definitively test as NICER coverage of observation 3 was not possible (and NuSTAR coverage was also not possible).

4.2. *IXPE Power Colors and Hue*

Heil et al. (2015a) showed that the evolution of the power spectrum is a more reliable diagnostic of state than the flux spectrum. In analogy to spectral colors, they therefore defined power colors (PCs) as a way to track the shape of the power spectrum with only a few numbers. They defined PC1 as the power spectrum integrated over the 0.25–2 Hz frequency range divided by the integral over the 0.0039–0.03 Hz range. Similarly, they defined PC2 as the 0.031–0.25 Hz integral divided by the 2–16 Hz integral. They showed that, on a plot of PC2 versus PC1, all sources follow the same oval shaped 'color wheel'. The evolution around the wheel is clockwise in the outburst rise and anti-clockwise on the decay back to quiescence. Spectral state can therefore be defined purely by the position of the source on this color wheel, which can be parameterized by a single 'hue' angle – named in direct analogy to a color wheel. The hue is calculated by nominating a center of the color wheel (PC1=4.51920, PC2=0.453724) and then finding the vector that points (in log space) from that center to the (PC1,PC2) point of the observation in question. The hue is then the clockwise angle from a vector in the $(-1, 1)$ direction to the vector calculated for the specific observation.

Table 2 quotes the hue angle calculated (by following the Heil et al. 2015b method exactly and employing $T_{\text{seg}} = 256$ s for all observations) for each observation using the co-spectrum in two different energy bands. The first, hue$_{(2-8)}$, is the full 2–8 keV energy band, which provides the best signal to noise. However, Heil et al. (2015a) based their classification on power spec-
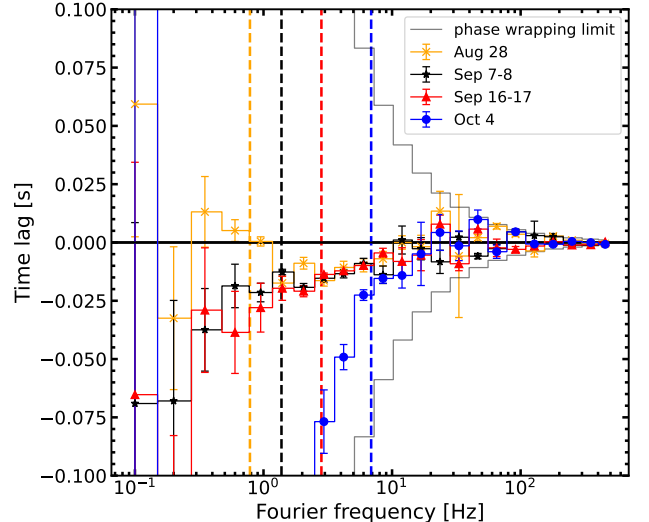
Figure 6. Time lag between 2–5 and 0.5–1 keV bands as a function of the Fourier frequency for NICER observations before (Aug 28, orange crosses) and during the first (Sept 7, black stars), second (Sept 16–17, red triangles), and fourth (Oct 4, blue circles) IXPE observations. Positive lag corresponds to hard photons lagging soft photons. The QPO frequencies are marked by the dashed vertical lines. The maximum and minimum measurable time lags (the phase-wrapping limits) are also shown (gray stepped line).

tra of the 2–13 keV energy band of the RXTE proportional counter array (which had an effective area peaking at ∼10 keV). To account for the harder band pass of RXTE, Wang et al. (2022) used the 4.8–9.6 keV energy band to unify their analysis of NICER data with the original RXTE analysis of Heil et al. (2015a). To follow suit, we therefore select the 5–8 keV band pass of IXPE and quote the results in the table as hue$_{(5-8)}$. We see this as the more reliable measurement when signal to noise is sufficiently high. However, the 5–8 keV hue is completely unconstrained for observations 4 and 5 (i.e. the uncertainty estimate is $\pm 180°$). We note that the two bands yield similar results for the first three observations, and so tentatively use the 2–8 keV hue for the final two.

Heil et al. (2015a) defined the hard state as hue$< 140°$ and the HIMS as $140° <$hue$< 220°$. Observation 1 is therefore on the border between the two states, Obs. 2–4 are firmly in the HIMS, and observation 5 is consistent within uncertainties with the HIMS or SIMS. Other than a hue $> 220°$, the onset of the SIMS is also associated with a sharp drop in total rms variability amplitude (Belloni 2010). We do not see such a drop here (the rms is comparable within uncertainty between observations 4 and 5), and so conclude that observation 5 is in the HIMS, at least according to its X-ray timing properties.
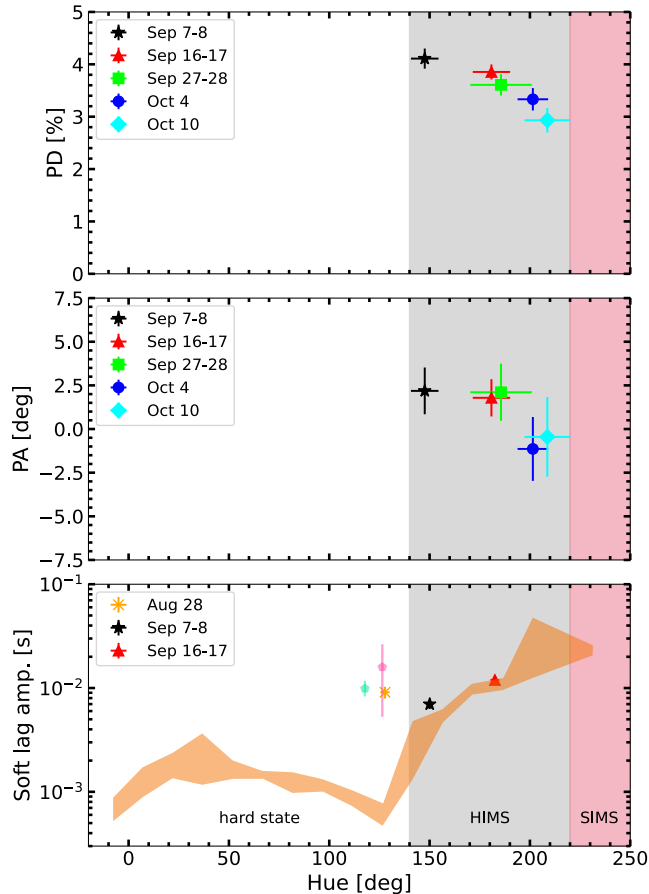
Figure 7. PD (top), PA (middle) in the 2–8 keV range, and soft lag amplitude (bottom) as a function of power spectral hue. The top two panels are made entirely with IXPE data and the bottom panel entirely with NICER data. The soft lag amplitude is averaged from the time lag versus frequency plots in Figure 6, and the same symbols and colors are employed. The orange shaded area depicts the average over eight sources that Wang et al. (2022) found to follow a common trend. The two outliers to that trend are also plotted: MAXI J1803−298 (turquoise pentagon) and EXO 1846−031 (pink pentagon).

4.3. *NICER Time Lags*

Figure 6 shows the time lag as a function of Fourier frequency ν for four NICER observations. Lags are measured using the cross-spectrum (van der Klis et al. 1987) between the 2–5 and 0.5–1 keV light curves. We use a time bin duration of $dt = 0.001$ s, a segment length of $T_{\rm seg} = 10$ s, and a re-binning factor of $c = 1.4$. We obtain the time lag by dividing the argument of the cross spectrum by $2\pi\nu$, employing the convention that positive lag corresponds to the harder band lagging the softer band. We also plot the phase-wrapping limits $\pm 1/(2\nu)$ (gray stepped line), which represent the maximum and minimum measurable lags. The errors on the

lags are calculated using the coherence (Uttley et al. 2014).

We take steps to circumvent the affects of NICER dead-time, which causes spurious anti-correlations between energy bands due to the detector sensitivity becoming anti-correlated with count rate on time scales comparable to or shorter than the dead-time. This effect is usually negligible in NICER due to its small dead-time. However, Swift J1727.8–1613 is exceptionally bright and NICER is currently suffering from solar light leaking in to the detectors, meaning that the spurious anti-correlation dominates on short ($\lesssim 0.1$ s) timescales if standard methods are employed. To circumvent this effect, we use one set of detectors to extract the hard band light curve, and another to extract the soft band light curve. We require that no MPUs are used in both light curves because telemetry saturation occurs per MPU and thus introduces spurious anti-correlations between different FPMs within the same MPU. We confirm that this procedure works as expected for the observations plotted in Figure 6 by confirming that it returns time lags consistent with zero between full band light curves extracted from these two sets of detectors.

We see that soft (negative) lags are visible in Figure 6 for a range of Fourier frequencies. To compare these observations to the wider population, we calculate an average soft lag for each, following the exact procedure detailed in Wang et al. (2022)'s population study. This involves averaging the time lag, weighted by the uncertainty, in a frequency range spanning from a minimum $\nu_{\rm min}$ to a maximum $\nu_{\rm max}$, ignoring any frequencies in this range dominated by the QPO (according to a multi-Lorentzian fit to the NICER power spectrum). $\nu_{\rm min}$ is the lowest frequency with a negative time lag. The range $\nu_{\rm min}$ to $\nu_{\rm max}$ is defined as the range of consecutive frequencies in which the phase lag is 1) consistent within 1σ uncertainty with being negative, and 2) larger (less negative) than $-\pi/2$. The latter stipulation is to avoid the average being biased by phase-wrapping at high frequencies where the lag is at risk of being consistent within uncertainties with the phase-wrapping limit (phase lag of $\pm\pi$).

Figure 7 (bottom) shows the resulting average soft lag amplitude for three of the NICER observations, plotted against 4.8–9.6 keV power spectral hue (see Section 4.2). The two measurements in the HIMS (black star and red triangle) are consistent with the common trend followed by eight of the ten sources in the Wang et al. (2022) sample (orange shaded area). In contrast, the one measurement in the hard state (orange cross) lies far from the common trend, but is remarkably consistent with the two outliers identified by Wang et al. (2022)
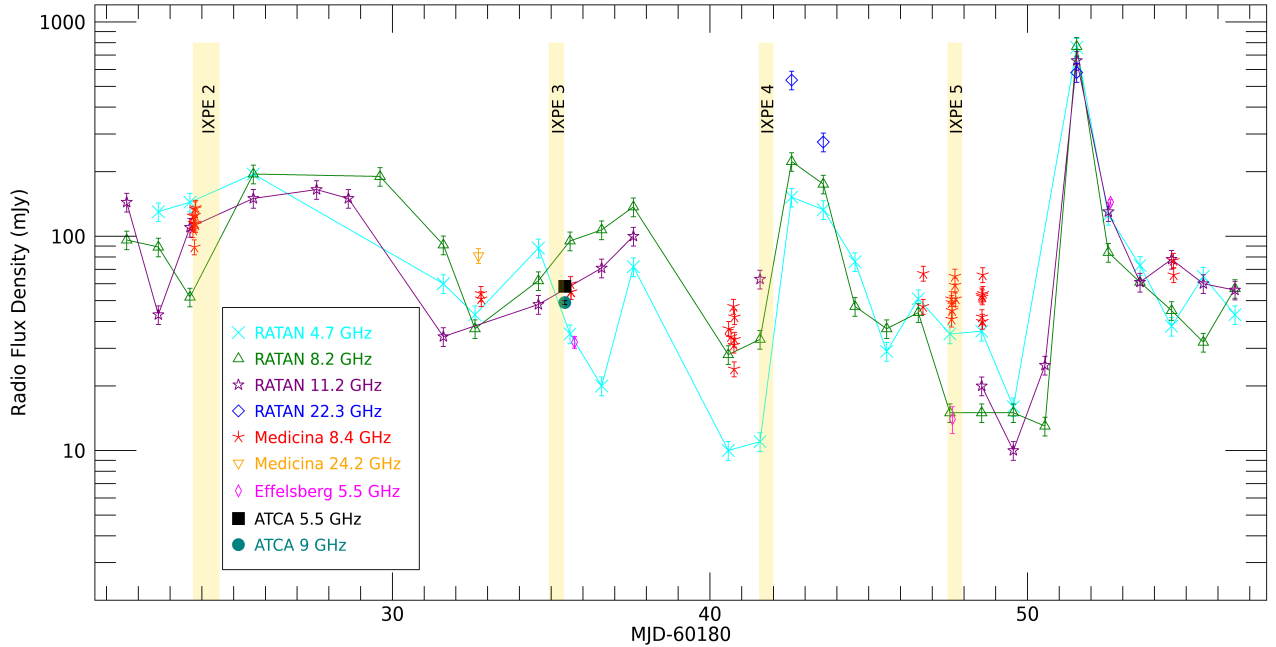
Figure 8. Evolution of the radio flux density in the time period encompassing IXPE observations 2–5. Facilities and frequency bands are as labeled.

(pentagonal markers). These outliers correspond to two sources. One, MAXI J1803−298, has only one observation whereas the other, EXO 1846−031, has a second observation at hue$\approx 200°$ with a large soft lag of ≈ 100 ms. We do not plot an average soft lag amplitude for the Oct 4 observation. This is because the phase lag of the Oct 4 observation switches from positive in the first frequency bin to $< -\pi/2$ in the second frequency bin; i.e. $\nu_{max} = \nu_{min}$ due to the phase-wrapping limit stipulated in the procedure described above. When we ignore the phase-wrapping limit, we measure an average soft lag amplitude of 35 ± 3 ms, which is consistent with the common trend (i.e. orange shaded area). However, we choose not to include the result in Figure 7 because it is calculated using different assumptions to all of the other observations considered. Above the soft lags, we plot 2–8 keV PD (top) and PA (middle) for the five IXPE observations. For observations 1–3, we use the 5–8 keV IXPE hue, which agrees very well with the 4.8–9.6 keV NICER hue for observations 1 and 2. For observations 4–5, we are instead limited to the 2–8 keV IXPE hue. We see that the five IXPE observations span the entire HIMS.

4.4. *Radio Evolution*

Figure 8 shows the radio light curve compiled from observations by RATAN-600, ATCA, Medicina and Effelsberg. The radio flux density was highly variable, with the Medicina observations in particular revealing short timescale variability. We see that mini-flares fol-

lowed IXPE observations 2 and 3. A larger flare was observed after IXPE observation 4, consistent with the flare detected by the Very Large Array at the same time (Miller-Jones et al. 2023a). Such a flare often marks the transition to the SIMS, accompanied by the onset of transient ejections, Type-B QPOs and preceding the eventual transition to the soft state (Fender et al. 2004; Homan et al. 2020). However, the transition to the SIMS did not occur, and the radio flux stabilized by the time of IXPE observation 5. An even larger radio flare was then observed in the days after observation 5. This flare may be associated with a discrete ejection and the transition to the SIMS. We see in Figure 1 that the X-ray spectrum did indeed continue to soften after the final IXPE observation, and is likely in the soft state at the time of writing. However, NICER and IXPE were Sun constrained by this time, precluding detailed determination of the X-ray spectral and timing properties.

We are additionally able to measure polarization at 5.5 and 9 GHz for the ATCA observation, which was partly simultaneous with IXPE observation 3. We use the unpolarized source PKS B1934−638 to solve antenna leakages (D-terms), and exclude the distant antenna CA06, which is located 6 km from the relatively compact core of the array. We measure linear polarization with a PD of $7\% \pm 2\%$ and $4\% \pm 2\%$ at 5.5 and 9 GHz respectively. No significant circular polarization was detected, with a 3σ upper-limit of 0.1% on Stokes V at both frequencies. With the CASA task `qufromgains`, we determine a PA of

$-7°.8 \pm 1°.5$ at 5.5 GHz and $-1°.7 \pm 0°.5$ at 9 GHz. We then determine the PA intrinsic to the source, the electric vector position angle (EVPA), by accounting for Faraday rotation, which is the wavelength-dependent rotation of the polarization vector that occurs as the emission propagates from the source to the observer. The EVPA relates to the PA measured at different wavelengths λ as EVPA $= \text{PA}(\lambda) - \text{RM}\lambda^2$, where RM is rotation measure. We find RM$= -55 \pm 20 \, \text{rad} \, \text{m}^{-2}$, yielding an EVPA of $2° \pm 2°$, consistent with the X-ray PA.

5. DISCUSSION

We have tracked the X-ray polarization of Swift J1727.8–1613 across a hard to soft state transition with five IXPE observations. This is the first time such an analysis has been possible for a transient X-ray binary. Our observations cover the entire HIMS, with the first observation coinciding with the transition from the hard state and the fifth close to the transition to the SIMS. This is indicated by the track the source followed on the HID (Figure 1c), the evolution of the power spectrum including QPOs with frequency evolving from $\approx 1.3 - 8$ Hz (Figures 5 and 7), and by the detection of radio flares before and after observation 5 (Figure 8).

Whereas the X-ray PA remains constant throughout the transition, the PD slowly decreases with time (with 3.5 σ confidence, Figure 3). The PD appears to increase with energy in all observations (Figure 4), but we can only state this with $> 3 \sigma$ statistical confidence for observations 2, 3, and 5. The slope of this energy dependence also appears to grow steeper as the spectrum softens, although only with 2.6 σ confidence. The PD at 5 keV is consistent with remaining constant in time. It is therefore possible that the PD of the corona is constant in time, and the overall PD is reducing only because the disk is coming further into the IXPE bandpass as its temperature increases. Such a reduction will happen if the disk is polarized perpendicular to the corona (or unpolarized), and this scenario would explain the reduction in PD occurring only at lower energies. This picture can be tested using spectro-polarimetric fits involving other observatories such as NICER and NuSTAR, which provide the spectral bandwidth that IXPE lacks. Such a study is beyond the scope of this paper, and we will leave it to future work. If the corona does have a constant PD and PA, this indicates that its aspect ratio H/R remains constant throughout the transition, even if its radial extent is shrinking as in the truncated disk model. Alternatively, or additionally, the reduction in PD could be driven by the corona itself, perhaps from

the aspect ratio slightly tending closer to unity (i.e. getting closer to spherical) during the transition.

We observe significant evolution in the spectral and timing properties of Swift J1727.8–1613 during the HIMS, in line with known phenomenology (e.g. Belloni 2010). The observed evolution of X-ray binaries is thought to be driven by changes in the geometry of the accretion disk and X-ray corona. There is much uncertainty as to the shape of the corona. The shapes that have been discussed in the literature can be grouped into two main classes: flattened in the disk plane (radially extended; Haardt & Maraschi 1991; Esin et al. 1997; Poutanen et al. 1997), or confined to a region around the disk axis, along the jet (vertically extended; Kylafis et al. 2008; Reig & Kylafis 2015; Kara et al. 2019; Wang et al. 2021). Some models expect the disk to be truncated in the hard state and to move towards the BH during the transition, whereas other studies infer the disk to already be at the ISCO in the bright hard state (e.g. García et al. 2015; Liu et al. 2023a). The X-ray spectrum alone can be explained in both scenarios, either with a single Comptonized spectrum and a broad iron line dominated by emission from close to the ISCO (e.g. Parker et al. 2014), or several Comptonized components from a stratified extended medium and a narrower iron line emitted from a truncated disk (Frontera et al. 2001; Ibragimov et al. 2005; Shidatsu et al. 2011; Zdziarski et al. 2021).

X-ray timing information enables orthogonal constraints. In particular, soft lags (0.5–1 keV lagging 2–5 keV) seen at high Fourier frequencies ($\gtrsim 1$ Hz) have been attributed to reverberation. We compare our X-ray polarization measurements with soft lag measurements extracted from simultaneous NICER data (Figure 7). We find that the soft lags are fairly long ($\gtrsim 10$ ms). In the simplest interpretation whereby the lags are driven only by light-crossing delays, this implies a highly vertically extended corona ($H/R \gg 1$) as the only means of there being a large enough physical distance between illuminator and reflector (Wang et al. 2021; Lucchini et al. 2023). However, here we find that the X-ray polarization aligns with both the $\sim$230 GHz polarization measured in the hard state (on Sep 3–4; Vrtilek et al. 2023), and with the 7.25 GHz polarization measured quasi-simultaneously with observation 3 (Section 4.4). Since the radio polarization often aligns with the jet direction in the hard state (e.g., Corbel et al. 2000; Hannikainen et al. 2000; Russell et al. 2015, indicating that the jet magnetic field is primarily toroidal), this implies that the corona is instead radially extended.

We see the most likely resolution to this apparent discrepancy between timing and polarization being that

the corona is radially extended, but that the soft lags in the HIMS are dominated by effects other than pure light-crossing delays. Such effects have been considered extensively in the literature. For example, interference between variable Comptonized signals emitted primarily from different regions of a stratified corona (Veledina 2018; Mahmoud et al. 2019), and/or between variable disk and corona signals (Rapisarda et al. 2017, Uttley & Malzac in prep). These effects have also been used to explain the complex, energy-dependent evolution of the power spectrum (Veledina 2016; Rapisarda et al. 2016, 2017; Chainakun et al. 2021). Although light-crossing delays must be present at some level, we suggest that they are not the dominant process in the HIMS, at least for soft X-rays in the frequency ranges accessible to current missions. In contrast, light-crossing delays could still potentially be the dominant mechanism, even in the HIMS, in the iron line energy range, and in frequency ranges ($\gtrsim 100$ Hz) only available to future high-throughput space missions (Zhang et al. 2019; Ray et al. 2019). Our conclusion remains relatively tentative until it can be confirmed or falsified by the publication of resolved images of the Swift J1727.8–1613 radio jet, since it hinges on the assumption that the intrinsic radio polarization is aligned with the jet.

The long soft lags we observe in the HIMS are representative of what is observed for the general BH X-ray binary population (Wang et al. 2022). However, we also measure a similarly long soft lag in the hard state (Figure 7). Since the Swift J1727.8–1613 lags are very similar to those of two outliers in the Wang et al. (2022) population study, our favored explanation is that these outliers and Swift J1727.8–1613 are actually members of a subset of the X-ray binary population that happened to be under-represented in the NICER archive until now. Although there are 10 sources in the Wang et al. (2022) sample, the hard state is only represented by three sources (reflecting the difficulty of quickly slewing to a source at the onset of an outburst), and is dominated by one (MAXI J1820+070, which evolved exceptionally slowly). Therefore, it is plausible that a large subset of X-ray binaries exhibit long soft lags already in the hard state, but that none of them had been observed in the hard state by NICER at the time of the Wang et al. (2022) analysis.

We can only speculate as to the physical property that separates the two subsets of soft lag evolution with hue. Perhaps the difference is orbital inclination angle. There is evidence that inclination influences other timing properties (Motta et al. 2015; van den Eijnden et al. 2017). Misalignment between the BH spin and orbital axes, which was suggested to be large in MAXI J1820+070

(Poutanen et al. 2022; Thomas et al. 2022), could also be a factor. NICER monitoring of sources with a variety of orbital and jet parameters is required for a definitive test.

The constancy of PA we observe here rules out any interpretation of the transition that predicts the PA to flip by 90° during the HIMS. Such a flip would result from the corona switching from radially extended in the hard state ($H/R < 1$) to vertically extended ($H/R \gg 1$) by the end of the HIMS. This scenario was previously plausible, since earlier IXPE results had indicated the corona to be radially extended in the hard state, and interpretation of the long observed soft lags as pure light-crossing delays requires a very large vertical corona height in the HIMS. This picture also provided a ready interpretation of the discrete jet ejection typically detected soon after the soft lag increase as the corona itself being fired away from the BH (Wang et al. 2021). Indeed, it is remarkable that the X-ray polarization does not seem to react to the radio flare between observations 4 and 5, which presumably results from an ejection of coronal plasma. The QPO model of Méndez et al. (2022) instead predicts the corona to switch from vertically extended in the hard state to radially extended in the HIMS. This is not only ruled out by our observations here of constant PA across the transition, but also by earlier observations of the X-ray polarization aligning with the jet (Krawczynski et al. 2022).

6. CONCLUSIONS

We have made the first X-ray polarimetric observations of a BH X-ray binary during a state transition. With five IXPE observations of Swift J1727.8–1613 spanning the HIMS, we find that the PD gradually decreases from ~4% at the start of the HIMS to ~3% at the end, and the PA remains in the North-South direction throughout. The PA aligns with sub-mm polarization measured ~ 4 days before the first IXPE observation, and also with the 7.25 GHz radio polarization that we measure quasi-simultaneously with the third IXPE observation. Using the radio PA as a proxy for the jet position angle, this implies that the corona remains radially extended (flattened in the plane of the disk) throughout the transition. This conclusion can be definitively tested upon the publication of resolved radio images.

We find that the PA is consistent with being independent of energy, whereas the PD increases with energy (although only with $> 3\,\sigma$ statistical significance for three of the five observations). These properties are very similar to Cyg X-1 in the hard state.

We detect Type-C QPOs with centroid frequency increasing from ≈ 1.3 Hz in the first observation to ≈ 8 Hz

in the fifth. We also measure long soft lags (0.5–1 keV lagging 2–5 keV photons) with NICER of $\gtrsim 10$ ms, which would require a strongly vertically extended corona to be explained purely by light-crossing delays. Our polarization results therefore imply that the soft lags in the HIMS are dominated by processes other than pure light-crossing delays. We also find that the soft lags of Swift J1727.8–1613 do not evolve with state as expected from earlier studies, indicating that it belongs to a sub-population that was under-represented in previous samples.

Facilities: IXPE, MAXI, NICER, RATAN-600, Medicina, ATCA, Effelsberg

Software: ixpeobssim (Baldini et al. 2022), xspec (Arnaud 1996), stingray (Huppenkothen et al. 2019a,b; Bachetti et al. 2023), casa (CASA Team et al. 2022), sdi (Egron et al. 2017)

APPENDIX

A. SPECTRAL AND CALIBRATION PARAMETERS

Table 3 lists the spectral and calibration parameters used for our spectro-polarimetric fits in Section 3. The spectral parameters are well constrained, except for the power law in observations 4–5. Here, the uncertainties are large due to trade offs with the `diskbb` component in the relatively narrow IXPE band pass. Most calibration parameters are consistent within uncertainties across all observations. However, we were unable to find an acceptable fit when tying all of them to be identical for all observations. There are likely two effects combining to cause this. First, the changing flux and spectral shape of the source could have caused subtly different calibration issues for each observation. This could be due to a known charging effect on the detector gain that depends on the source count rate. Second, the model is over-simplified and so to some extent the gain fit will be fitting real features (e.g. the relativistically broadened iron line), which will be changing in shape and strength from one observation to the next. We note that the gain fit (or a similar procedure) is required to simultaneously fit IXPE data with data from other observatories such as NICER or

Table 3. Spectral (top) and calibration (bottom) parameters used in the `polconst` spectro-polarimetric fits. Those used for the `pollin` models are identical within uncertainties. The constant accounts for the different absolute flux calibration of the different DUs. We utilize the `gain fit` functionality of XSPEC. This scales the photon energy to $E' = E/$slope $-$ offset. Thus the original gain scale is recovered for slope=1 and offset=0.

		Obs 1	Obs 2	Obs 3	Obs 4	Obs 5
$kT_{\rm in}$	keV	-	-	-	$1.029^{+0.025}_{-0.006}$	$0.993^{+0.020}_{-0.005}$
$\mathtt{norm_d}$		-	-	-	4793^{+248}_{-410}	4959^{+179}_{-211}
Γ		$1.80^{+0.02}_{-0.01}$	2.26 ± 0.01	$2.57^{+0.01}_{-0.02}$	$1.78^{+0.57}_{-0.70}$	$1.78^{+0.73}_{-0.82}$
$\mathtt{norm_{po}}$		33.7 ± 0.6	59.8 ± 0.6	$77.7^{+0.6}_{-2.2}$	11^{+27}_{-9}	8^{+23}_{-6}
constant	DU1	1	1	1	1	1
slope	DU1	0.9402 ± 0.0020	0.9414 ± 0.0016	0.9354 ± 0.0025	0.9682 ± 0.0074	0.9504 ± 0.0141
offset	DU1	0.0558 ± 0.0049	0.0584 ± 0.0037	0.1116 ± 0.0056	0.0505 ± 0.0096	0.0536 ± 0.0169
constant	DU2	0.9781 ± 0.0014	0.9789 ± 0.0010	0.9780 ± 0.0014	0.9788 ± 0.0015	0.9783 ± 0.0016
slope	DU2	0.9353 ± 0.0020	0.9329 ± 0.0016	0.9416 ± 0.0025	0.9673 ± 0.0073	0.9455 ± 0.0140
offset	DU2	0.0551 ± 0.0050	0.0891 ± 0.0038	0.1301 ± 0.0057	0.0593 ± 0.0094	0.0629 ± 0.0169
constant	DU3	0.9208 ± 0.0013	0.9211 ± 0.0010	0.9192 ± 0.0014	0.9207 ± 0.0014	0.9147 ± 0.0015
slope	DU3	0.9419 ± 0.0020	0.9400 ± 0.0016	0.9555 ± 0.0025	0.9722 ± 0.0074	0.9518 ± 0.0014
offset	DU3	0.0860 ± 0.0050	0.1034 ± 0.0038	0.1038 ± 0.0055	0.0823 ± 0.0097	0.0664 ± 0.0158

NuSTAR (e.g. Svoboda et al. 2023), indicating that the need for the gain fit is not purely down to the model being over-simplified.

REFERENCES

Arévalo, P., & Uttley, P. 2006, MNRAS, 367, 801, doi: 10.1111/j.1365-2966.2006.09989.x

Arnaud, K. A. 1996, in ASP Conf. Ser., Vol. 101, Astronomical Data Analysis Software and Systems V, ed. G. H. Jacoby & J. Barnes (San Francisco: Astron. Soc. Pac.), 17–20

Bachetti, M., Harrison, F. A., Cook, R., et al. 2015, ApJ, 800, 109, doi: 10.1088/0004-637X/800/2/109

Bachetti, M., Huppenkothen, D., Khan, U., et al. 2023, StingraySoftware/stingray: Version 1.1.2, v1.1.2, Zenodo, doi: 10.5281/zenodo.7970570

Baldini, L., Barbanera, M., Bellazzini, R., et al. 2021, Astroparticle Physics, 133, 102628, doi: 10.1016/j.astropartphys.2021.102628

Baldini, L., Bucciantini, N., Lalla, N. D., et al. 2022, SoftwareX, 19, 101194, doi: 10.1016/j.softx.2022.101194

Bambi, C., Brenneman, L. W., Dauser, T., et al. 2021, SSRv, 217, 65, doi: 10.1007/s11214-021-00841-8

Barret, D., & Vaughan, S. 2012, ApJ, 746, 131, doi: 10.1088/0004-637X/746/2/131

Belloni, T. M. 2010, Lecture Notes in Physics, 794, 53, doi: 10.1007/978-3-540-76937-8_3

Bollemeijer, N., Uttley, P., Buisson, D., et al. 2023, The Astronomer's Telegram, 16247, 1

Bright, J., Farah, W., Fender, R., et al. 2023, The Astronomer's Telegram, 16228, 1

CASA Team, Bean, B., Bhatnagar, S., et al. 2022, PASP, 134, 114501, doi: 10.1088/1538-3873/ac9642

Casella, P., Belloni, T., & Stella, L. 2005, ApJ, 629, 403, doi: 10.1086/431174

Chainakun, P., Luangtip, W., Young, A. J., Thongkonsing, P., & Srichok, M. 2021, A&A, 645, A99, doi: 10.1051/0004-6361/202039090

Corbel, S., Fender, R. P., Tzioumis, A. K., et al. 2000, A&A, 359, 251, doi: 10.48550/arXiv.astro-ph/0003460

De Marco, B., Ponti, G., Muñoz-Darias, T., & Nandra, K. 2015, ApJ, 814, 50, doi: 10.1088/0004-637X/814/1/50

De Marco, B., Zdziarski, A. A., Ponti, G., et al. 2021, A&A, 654, A14, doi: 10.1051/0004-6361/202140567

De Marco, B., Ponti, G., Petrucci, P. O., et al. 2017, MNRAS, 471, 1475, doi: 10.1093/mnras/stx1649

Di Marco, A., Soffitta, P., Costa, E., et al. 2023, AJ, 165, 143, doi: 10.3847/1538-3881/acba0f

Done, C., Gierlinski, M., & Kubota, A. 2007, A&A, 15, 1, doi: 10.1007/s00159-007-0006-1

Dovciak, M., Steiner, J. F., Krawczynski, H., & Svoboda, J. 2023, The Astronomer's Telegram, 16084, 1

Draghis, P. A., Miller, J. M., Homan, J., et al. 2023, The Astronomer's Telegram, 16219, 1

Dunn, R. J. H., Fender, R. P., Körding, E. G., Belloni, T., & Cabanac, C. 2010, MNRAS, 403, 61, doi: 10.1111/j.1365-2966.2010.16114.x

Eardley, D. M., Lightman, A. P., & Shapiro, S. L. 1975, ApJL, 199, L153, doi: 10.1086/181871

Egron, E., Pellizzoni, A., Iacolina, M. N., et al. 2017, MNRAS, 470, 1329, doi: 10.1093/mnras/stx1240

Esin, A. A., McClintock, J. E., & Narayan, R. 1997, ApJ, 489, 865, doi: 10.1086/304829

Fabian, A. C., Rees, M. J., Stella, L., & White, N. E. 1989, MNRAS, 238, 729

Fender, R. P., Belloni, T. M., & Gallo, E. 2004, MNRAS, 355, 1105, doi: 10.1111/j.1365-2966.2004.08384.x

Ferrazzoli, R., Muleri, F., Lefevre, C., et al. 2020, JATIS, 6, 048002, doi: 10.1117/1.JATIS.6.4.048002

Frontera, F., Palazzi, E., Zdziarski, A. A., et al. 2001, ApJ, 546, 1027, doi: 10.1086/318304

Galeev, A. A., Rosner, R., & Vaiana, G. S. 1979, ApJ, 229, 318, doi: 10.1086/156957

García, J., & Kallman, T. R. 2010, ApJ, 718, 695, doi: 10.1088/0004-637X/718/2/695

García, J. A., Steiner, J. F., McClintock, J. E., et al. 2015, ApJ, 813, 84, doi: 10.1088/0004-637X/813/2/84

Gendreau, K. C., Arzoumanian, Z., Adkins, P. W., et al. 2016, in Proc. SPIE, Vol. 9905, Space Telescopes and Instrumentation 2016: Ultraviolet to Gamma Ray, 99051H, doi: 10.1117/12.2231304

Haardt, F., & Maraschi, L. 1991, ApJL, 380, L51, doi: 10.1086/186171

—. 1993, ApJ, 413, 507, doi: 10.1086/173020

Hannikainen, D. C., Hunstead, R. W., Campbell-Wilson, D., et al. 2000, ApJ, 540, 521, doi: 10.1086/309294

HEASARC. 2014, HEAsoft: Unified Release of FTOOLS and XANADU. http://ascl.net/1408.004

Heil, L. M., Uttley, P., & Klein-Wolt, M. 2015a, MNRAS, 448, 3339, doi: 10.1093/mnras/stv191

—. 2015b, MNRAS, 448, 3348, doi: 10.1093/mnras/stv240

Homan, J., Buxton, M., Markoff, S., et al. 2005, ApJ, 624, 295, doi: 10.1086/428722

Homan, J., Wijnands, R., van der Klis, M., et al. 2001, ApJS, 132, 377, doi: 10.1086/318954

Homan, J., Bright, J., Motta, S. E., et al. 2020, ApJL, 891, L29, doi: 10.3847/2041-8213/ab7932

Huppenkothen, D., Bachetti, M., Stevens, A., et al. 2019a, The Journal of Open Source Software, 4, 1393, doi: 10.21105/joss.01393

Huppenkothen, D., Bachetti, M., Stevens, A. L., et al. 2019b, ApJ, 881, 39, doi: 10.3847/1538-4357/ab258d

Ibragimov, A., Poutanen, J., Gilfanov, M., Zdziarski, A. A., & Shrader, C. R. 2005, MNRAS, 362, 1435, doi: 10.1111/j.1365-2966.2005.09415.x

Ingram, A., & van der Klis, M. v. d. 2013, MNRAS, 434, 1476, doi: 10.1093/mnras/stt1107

Ingram, A. R. 2012, PhD thesis, Durham University, UK

Ingram, A. R., & Motta, S. E. 2019, NewAR, 85, 101524, doi: 10.1016/j.newar.2020.101524

Kara, E., Steiner, J. F., Fabian, A. C., et al. 2019, Nature, 565, 198, doi: 10.1038/s41586-018-0803-x

Kawamura, T., Done, C., & Takahashi, T. 2023, MNRAS, 525, 1280, doi: 10.1093/mnras/stad2338

Kazanas, D., Hua, X., & Titarchuk, L. 1997, ApJ, 480, 735, doi: 10.1086/303991

Kennea, J. A., & Swift Team. 2023, GRB Coordinates Network, 34540, 1

Körding, E., & Falcke, H. 2004, A&A, 414, 795, doi: 10.1051/0004-6361:20031614

Kotov, O., Churazov, E., & Gilfanov, M. 2001, MNRAS, 327, 799, doi: 10.1046/j.1365-8711.2001.04769.x

Kraus, A., Krichbaum, T. P., Wegner, R., et al. 2003, A&A, 401, 161, doi: 10.1051/0004-6361:20030118

Kravtsov, V., Nitindala, A. P., Veledina, A., et al. 2023, The Astronomer's Telegram, 16245, 1

Krawczynski, H., Muleri, F., Dovčiak, M., et al. 2022, Science, 378, 650, doi: 10.1126/science.add5399

Kylafis, N. D., Papadakis, I. E., Reig, P., Giannios, D., & Pooley, G. G. 2008, A&A, 489, 481, doi: 10.1051/0004-6361:20079159

Liu, H., Bambi, C., Jiang, J., et al. 2023a, ApJ, 950, 5, doi: 10.3847/1538-4357/acca17

Liu, H. Y., Li, D. Y., Pan, H. W., et al. 2023b, The Astronomer's Telegram, 16210, 1

Lucchini, M., Mastroserio, G., Wang, J., et al. 2023, ApJ, 951, 19, doi: 10.3847/1538-4357/acd24f

Lyubarskii, Y. E. 1997, MNRAS, 292, 679, doi: 10.1093/mnras/292.3.679

Mahmoud, R. D., Done, C., & De Marco, B. 2019, MNRAS, 486, 2137, doi: 10.1093/mnras/stz933

Markoff, S., Nowak, M. A., & Wilms, J. 2005, ApJ, 635, 1203, doi: 10.1086/497628

Martocchia, A., & Matt, G. 1996, MNRAS, 282, L53, doi: 10.1093/mnras/282.4.L53

Matsuoka, M., Kawasaki, K., Ueno, S., et al. 2009, PASJ, 61, 999, doi: 10.1093/pasj/61.5.999

Matt, G., Perola, G. C., & Piro, L. 1991, A&A, 247, 25

Méndez, M., Karpouzas, K., García, F., et al. 2022, Nature Astronomy, 6, 577, doi: 10.1038/s41550-022-01617-y

Mereminskiy, I., Lutovinov, A., Molkov, S., et al. 2023, MNRAS, submitted, arXiv:2310.06697, doi: 10.48550/arXiv.2310.06697

Miller, J. M. 2007, ARA&A, 45, 441, doi: 10.1146/annurev.astro.45.051806.110555

Miller-Jones, J. C. A., Bahramian, A., Homan, J., et al. 2023a, The Astronomer's Telegram, 16271, 1

Miller-Jones, J. C. A., Sivakoff, G. R., Bahramian, A., & Russell, T. D. 2023b, The Astronomer's Telegram, 16211, 1

Miller-Jones, J. C. A., Bahramian, A., Orosz, J. A., et al. 2021, Science, 371, 1046, doi: 10.1126/science.abb3363

Miyamoto, S., & Kitamoto, S. 1991, ApJ, 374, 741, doi: 10.1086/170158

Miyamoto, S., Kitamoto, S., Mitsuda, K., & Dotani, T. 1988, Nature, 336, 450, doi: 10.1038/336450a0

Motta, S. E., Casella, P., Henze, M., et al. 2015, MNRAS, 447, 2059, doi: 10.1093/mnras/stu2579

Negoro, H., Serino, M., Nakajima, M., et al. 2023, GRB Coordinates Network, 34544, 1

Novikov, I. D., & Thorne, K. S. 1973, in Black Holes (Les Astres Occlus), ed. C. Dewitt & B. S. Dewitt (New York: Gordon and Breach), 343–450

Nowak, M. A., Vaughan, B. A., Wilms, J., Dove, J. B., & Begelman, M. C. 1999, ApJ, 510, 874, doi: 10.1086/306610

Ott, M., Witzel, A., Quirrenbach, A., et al. 1994, A&A, 284, 331

Palmer, D. M., & Parsotan, T. M. 2023, The Astronomer's Telegram, 16215, 1

Parker, M. L., Wilkins, D. R., Fabian, A. C., et al. 2014, MNRAS, 443, 1723, doi: 10.1093/mnras/stu1246

Poutanen, J. 2002, MNRAS, 332, 257, doi: 10.1046/j.1365-8711.2002.05272.x

Poutanen, J., & Fabian, A. C. 1999, MNRAS, 306, L31, doi: 10.1046/j.1365-8711.1999.02735.x

Poutanen, J., Krolik, J. H., & Ryde, F. 1997, MNRAS, 292, L21

Poutanen, J., & Svensson, R. 1996, ApJ, 470, 249, doi: 10.1086/177865

Poutanen, J., Veledina, A., & Zdziarski, A. A. 2018, A&A, 614, A79, doi: 10.1051/0004-6361/201732345

Poutanen, J., Veledina, A., Berdyugin, A. V., et al. 2022, Science, 375, 874, doi: 10.1126/science.abl4679

Psaltis, D., Belloni, T., & van der Klis, M. 1999, ApJ, 520, 262, doi: 10.1086/307436

Ramsey, B. D., Bongiorno, S. D., Kolodziejczak, J. J., et al. 2022, JATIS, 8, 024003, doi: 10.1117/1.JATIS.8.2.024003

Rapisarda, S., Ingram, A., Kalamkar, M., & van der Klis, M. 2016, MNRAS, 462, 4078, doi: 10.1093/mnras/stw1878

Rapisarda, S., Ingram, A., & van der Klis, M. 2017, MNRAS, 469, 2011, doi: 10.1093/mnras/stx991

Ratheesh, A., Dovčiak, M., Krawczynski, H., et al. 2023, arXiv e-prints, arXiv:2304.12752, doi: 10.48550/arXiv.2304.12752

Ray, P. S., Arzoumanian, Z., Ballantyne, D., et al. 2019, arXiv e-prints, arXiv:1903.03035, doi: 10.48550/arXiv.1903.03035

Reig, P., & Kylafis, N. D. 2015, A&A, 584, A109, doi: 10.1051/0004-6361/201527151

Remillard, R., & McClintock, J. 2006, ARA&A, 44, 49, doi: 10.1146/annurev.astro.44.051905.092532

Reynolds, C. S., Young, A. J., Begelman, M. C., & Fabian, A. C. 1999, ApJ, 514, 164, doi: 10.1086/306913

Rodriguez Cavero, N., Marra, L., Krawczynski, H., et al. 2023, ApJL, in press, arXiv:2305.10630, doi: 10.48550/arXiv.2305.10630

Russell, T. D., Miller-Jones, J. C. A., Curran, P. A., et al. 2015, MNRAS, 450, 1745, doi: 10.1093/mnras/stv723

Shakura, N. I., & Sunyaev, R. A. 1973, A&A, 24, 337

Shidatsu, M., Ueda, Y., Tazaki, F., et al. 2011, PASJ, 63, 785. https://arxiv.org/abs/1105.3586

Soffitta, P., Baldini, L., Bellazzini, R., et al. 2021, AJ, 162, 208, doi: 10.3847/1538-3881/ac19b0

Stern, B. E., Poutanen, J., Svensson, R., Sikora, M., & Begelman, M. C. 1995, ApJL, 449, L13, doi: 10.1086/309617

Sunyaev, R. A., & Truemper, J. 1979, Nature, 279, 506, doi: 10.1038/279506a0

Sunyaev, R. A., Mereminskiy, I. A., Molkov, S. V., et al. 2023, The Astronomer's Telegram, 16217, 1

Svoboda, J., Dovčiak, M., Steiner, J. F., et al. 2023, ApJ, in press, arXiv:2309.10813, doi: 10.48550/arXiv.2309.10813

Tetarenko, B. E., Sivakoff, G. R., Heinke, C. O., & Gladstone, J. C. 2016, ApJS, 222, 15, doi: 10.3847/0067-0049/222/2/15

Thomas, J. K., Charles, P. A., Buckley, D. A. H., et al. 2022, MNRAS, 509, 1062, doi: 10.1093/mnras/stab3033

Thorne, K. S., & Price, R. H. 1975, ApJL, 195, L101, doi: 10.1086/181720

Ursini, F., Matt, G., Bianchi, S., et al. 2022, MNRAS, 510, 3674, doi: 10.1093/mnras/stab3745

Uttley, P., Cackett, E. M., Fabian, A. C., Kara, E., & Wilkins, D. R. 2014, A&A Rv, 22, 72, doi: 10.1007/s00159-014-0072-0

Uttley, P., Wilkinson, T., Cassatella, P., et al. 2011, MNRAS, 414, L60, doi: 10.1111/j.1745-3933.2011.01056.x

van den Eijnden, J., Ingram, A., Uttley, P., et al. 2017, MNRAS, 464, 2643, doi: 10.1093/mnras/stw2634

van der Klis, M. 1989, ARA&A, 27, 517, doi: 10.1146/annurev.aa.27.090189.002505

—. 2006, Advances in Space Research, 38, 2675, doi: 10.1016/j.asr.2005.11.026

van der Klis, M., Hasinger, G., Stella, L., et al. 1987, ApJL, 319, L13, doi: 10.1086/184946

van Straaten, S., van der Klis, M., di Salvo, T., & Belloni, T. 2002, ApJ, 568, 912, doi: 10.1086/338948

Veledina, A. 2016, ApJ, 832, 181, doi: 10.3847/0004-637X/832/2/181

—. 2018, MNRAS, 481, 4236, doi: 10.1093/mnras/sty2556

Veledina, A., Muleri, F., Dovciak, M., et al. 2023, ApJL, in press, arXiv:2309.15928. https://arxiv.org/abs/2309.15928

Vrtilek, S. D., Gurwell, M., McCollough, M., & Rao, R. 2023, The Astronomer's Telegram, 16230, 1

Wang, J., Mastroserio, G., Kara, E., et al. 2021, ApJL, 910, L3, doi: 10.3847/2041-8213/abec79

Wang, J., Kara, E., Lucchini, M., et al. 2022, ApJ, 930, 18, doi: 10.3847/1538-4357/ac6262

Weisskopf, M. C., Soffitta, P., Baldini, L., et al. 2022, JATIS, 8, 026002, doi: 10.1117/1.JATIS.8.2.026002

Wijnands, R., Homan, J., & van der Klis, M. 1999, ApJL, 526, L33, doi: 10.1086/312365

Zdziarski, A. A., Dziełak, M. A., De Marco, B., Szanecki, M., & Niedźwiecki, A. 2021, ApJL, 909, L9, doi: 10.3847/2041-8213/abe7ef

Zhang, S., Santangelo, A., Feroci, M., et al. 2019, Science China Physics, Mechanics, and Astronomy, 62, 29502, doi: 10.1007/s11433-018-9309-2